

***g*-factor engineering with InAsSb alloys toward zero band gap limit**

Yuxuan Jiang^{1,2,*}, Maksim Ermolaev³, Seongphill Moon^{4,5}, Gela Kipshidze³, Gregory Belenky³, Stefan Svensson⁶, Mykhaylo Ozerov⁴, Dmitry Smirnov⁴, Zhigang Jiang^{7,†} and Sergey Suchalkin^{3,‡}

¹*School of Physics and Optoelectronics Engineering, Anhui University, Hefei 230601, China*

²*Center of Free Electron Laser and High Magnetic Field, Anhui University, Hefei 230601, China*


³*Department of Electrical and Computer Engineering, Stony Brook University, Stony Brook, New York 11794, USA*

⁴*National High Magnetic Field Laboratory, Tallahassee, Florida 32310, USA*

⁵*Department of Physics, Florida State University, Tallahassee, Florida 32306, USA*

⁶*U.S. Army Research Directorate, Adelphi, Maryland 20783, USA*

⁷*School of Physics, Georgia Institute of Technology, Atlanta, Georgia 30332, USA*

 (Received 17 June 2023; revised 4 August 2023; accepted 23 August 2023; published 6 September 2023)

Band gap is known as an effective parameter for tuning the Landé g factor in semiconductors and can be manipulated in a wide range through the bowing effect in ternary alloys. In this work, using the recently developed virtual substrate technique, high-quality InAsSb alloys throughout the whole Sb composition range are fabricated and a large g factor of $g \approx -90$ at the minimum band gap of ~ 0.1 eV, which is almost twice that in bulk InSb, is found. Further analysis to the zero gap limit reveals a possible gigantic g factor of $g \approx -200$ with a peculiar relativistic Zeeman effect that disperses as the square root of magnetic field. Such a g -factor enhancement toward the narrow gap limit cannot be quantitatively described by the conventional Roth formula, as the orbital interaction effect between the nearly triply degenerated bands becomes the dominant source for the Zeeman splitting. These results may provide insights into realizing large g factors and spin-polarized states in semiconductors and topological materials.

DOI: [10.1103/PhysRevB.108.L121201](https://doi.org/10.1103/PhysRevB.108.L121201)

Landé g factor is a major material parameter describing the response of electron spins to an external magnetic field (B). In solid state physics, the long-standing interest in finding large g -factor materials originates from the peculiar spin-dependent transport and optical phenomena, which hold great promise for potential applications in spintronics [1,2], nonreciprocal spin photonics [3], and quantum information processing [4,5].

In III-V semiconductors, the electron g factor is known to observe the renowned Roth formula [6,7]

$$g = g_e - \frac{2}{3} \left(\frac{1}{E_g} - \frac{1}{\Delta + E_g} \right) E_P,$$

where $g_e \approx 2$, E_g , Δ , and E_P are the free electron g factor, the band gap, the spin-orbit coupling, and the Kane energy, respectively. The Roth formula is, in principle, a single-band theory, which explains the g -factor as a result of remote band perturbations [8]. A recent study further reveals the connection between the g factor and the Berry curvature of the bands due to the mixing of wave functions [9]. Therefore, it is natural to expect a large g factor in narrow band gap materials. Indeed, among all the binary III-V semiconductors, InSb has the smallest band gap and thus the largest g factor, $g \approx -52$ [10,11].

To further reduce the band gap, one can resort to ternary semiconductor InAsSb alloys, as the bowing effects can suppress the band gaps below those of their binary constituents [12]. Recent experiments have firmly established a strong negative bowing of the band gap with a bowing coefficient of ~ 0.8 eV [13,14], leading to a minimum band gap of 0.1 eV when the Sb composition is close to 63%. As a result, the theoretical estimation of the electron g factor based on the Roth formula reaches as high as $g = -117$, which is more than twice that in InSb [15,16]. Such a large tunable range of band gaps and g factors has rendered InAsSb alloy a promising platform for spintronics [15–17], topological phase engineering [18–20], and infrared (IR) optoelectronics [21–23].

However, there remain concerns about the high expectation value of g factors in InAsSb alloys toward the zero gap limit. On the one hand, the Roth formula is a single-band theory and fails to predict the correct result as the band gap reduces, and multiband theories such as the $\mathbf{k} \cdot \mathbf{p}$ model are necessary. Also, the experimental studies of g factors in the narrow or zero band gap region, particularly for Dirac materials, do not exhibit extraordinarily large g factors as expected [24–26]. On the other hand, there are technical difficulties in obtaining high-quality InAsSb alloys with the Sb composition close to 50%. Although in earlier works, InAsSb alloys with different alloy compositions were fabricated, they suffered from a large lattice mismatch between the alloy and substrate, which led to the relaxation of the bulk alloy and formation of numerous threading dislocations deteriorating the electronic properties [27,28]. The increased disorder, particularly in the

*yuxuan.jiang@ahu.edu.cn

†zhigang.jiang@physics.gatech.edu

‡sergey.suchalkin@stonybrook.edu

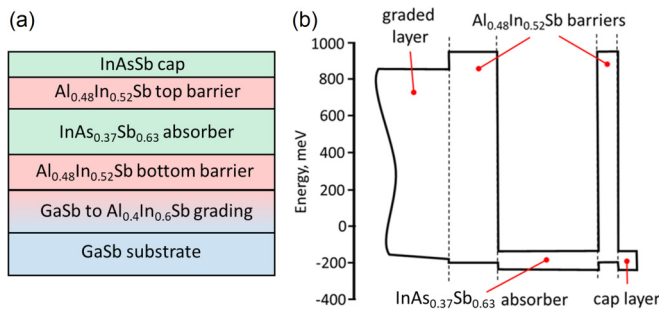


FIG. 1. (a) Structure layout of the InAs_{0.37}Sb_{0.63} sample. The InAsSb alloy (absorber) is sandwiched between the two Al_{0.48}In_{0.52}Sb barriers. (b) Schematic band alignment of the InAs_{0.37}Sb_{0.63} sample as an example. The zero energy corresponds to the top of the GaSb valence band.

intermediate composition range, can contribute to the extrinsic composition dependence of the key material parameters that determine the g factor in a bulk material, such as E_g , Δ , and E_p [29], and makes the experimental characterization of their intrinsic electronic property difficult.

Recent advances in the virtual substrate technique allow for the molecular beam epitaxy (MBE) growth of high-quality unstrained, unrelaxed InAsSb alloys in the whole composition range [14,30], providing a perfect opportunity for experimental studies of the material parameters and g factors in the narrow band gap region. In this work, we present a systematic investigation of the band structure evolution with the composition in InAsSb alloys via a combination of magnetoabsorption measurements and $\mathbf{k} \cdot \mathbf{p}$ calculations. We find that the Kane energy shows very little bowing effect across the entire composition range, but the g factor increases significantly as the band gap reaches the minimum. When $E_g \rightarrow 0$, the Landau levels (LLs) of the triply degenerated bands become fully relativistic (i.e., LL energy $\propto \sqrt{B}$) due to the dominant orbital interaction, and their relative wave-function mixing determines the spin states and energy spacing of the LLs. For a typical III-V (more generally, zinc-blende type) semiconductor, we find that these relativistic LLs are highly spin polarized along with maximized energy spacings, which could lead to a g factor of $g \approx -200$ at 1 T (vs $g \rightarrow -\infty$ based on the Roth formula), overwhelmingly larger than most of the two-band Dirac materials. Our findings may provide another perspective for g -factor engineering in future devices based on semiconductors and topological materials.

Five InAs_{1-x}Sb_x alloy samples are studied in this work, with $x = 0.09, 0.22, 0.44, 0.50, \text{ and } 0.63$. These samples are grown by solid-source MBE on undoped GaSb(100)

substrates. The $x = 0.50$ sample was grown using a VEECO Gen II MBE system in Army Research Laboratory, and the other samples were grown using a VEECO GEN930 MBE system in Stony Brook University. The growth process has been described previously in Ref. [14]. The core structure and band alignment of our InAs_{0.37}Sb_{0.63} sample are schematically shown in Fig. 1 as an example. Information on the core structures of these samples is summarized in Table I. In addition, samples with $x = 0.09, 0.22, \text{ and } 0.44$ are n doped (Te doped, $2 \times 10^{16} \text{ cm}^{-3}$), and samples with $x = 0.50$ and 0.63 are grown without intentional doping. To avoid the formation of two-dimensional electron “pockets” due to band bending at the boundaries of the InAsSb layer (absorber), the barriers and cap are p -doped to 10^{16} cm^{-3} . The three-dimensional character of the carrier motion in InAsSb is confirmed by magnetotransport measurements in tilted magnetic fields [14].

InAsSb alloy samples are then studied with magneto-IR spectroscopy, which is known for its accuracy in determining electronic band structures. The samples are placed inside a superconducting magnet at liquid-helium temperature (the effective temperature at the sample is measured to be $T = 5 \text{ K}$). The samples are illuminated with IR radiation in the Faraday configuration using a Bruker 80v Fourier-transform IR spectrometer. A composite Si bolometer is mounted behind the sample to detect the transmitted light signal at different magnetic fields.

Figure 2(a) shows the false color plot of the normalized transmission $T(B)/T(0 \text{ T})$ of the InAs_{0.50}Sb_{0.50} sample as a typical example. A series of absorption modes, which blueshift in energy with increasing magnetic fields, can be identified and attributed to LL transitions. The low-lying transitions are labeled with T_0 – T_5 . These modes originate from the same nonzero energy intercept as the magnetic field approaches zero, indicative of the nature of interband LL transitions. The energy intercept allows for direct readout of the band gap $E_g = 108 \text{ meV}$.

To quantitatively describe these LL transitions and extract other material parameters, we employ the well-established eight-band $\mathbf{k} \cdot \mathbf{p}$ model to fit the experimental results [24,27,31,32]. The model consists of several parameters, including E_g , Δ , E_p , the electron effective mass m^* , and the modified Luttinger parameters γ_1 , γ_2 , and γ_3 . To simplify the Hamiltonian, we first assume $\gamma_{1,2,3} = 0$. Meanwhile, we set $A_c = \hbar^2/2m^* - E_p(3E_g + 2\Delta)/6m_0E_g(E_g + \Delta) = 0$, where \hbar is the reduced Planck constant and m_0 is the free-electron mass, to avoid spurious solutions [33]. Finally, we focus on the Γ point LLs, which carry the dominant contributions to the observed optical transitions. With these

TABLE I. Composition and thickness of the core layers in the MBE-grown InAsSb samples of different Sb concentrations. The core layer structure is shown in Fig. 1(a).

Sb (%)	Grading (nm)	Bottom barrier (nm)	Absorber (nm)	Top barrier (nm)	Cap layer (nm)		
9	Not	N/A	Al ₈₀ Ga ₂₀ As _{6.2} Sb _{93.8}	500	InAs ₉₁ Sb ₉ 1000	Al ₈₀ Ga ₂₀ As _{6.2} Sb _{93.8} 200	InAs ₉₁ Sb ₉ 100
22	Al ₈₅ In ₁₅ Sb	1600	Al ₉₅ In _{4.5} Sb	500	InAs ₇₈ Sb ₂₂ 1000	Al ₉₅ In _{4.5} Sb 200	InAs ₇₈ Sb ₂₂ 100
44	Al ₆₀ In ₄₀ Sb	3000	Al ₆₈ In ₃₂ Sb	500	InAs ₅₆ Sb ₄₄ 1000	Al ₆₈ In ₃₂ Sb 200	InAs ₅₆ Sb ₄₄ 100
50	Al ₃₉ In ₆₁ Sb	2630	Al ₆₃ In ₃₇ Sb	250	InAs ₅₀ Sb ₅₀ 1500	Al ₆₃ In ₃₇ Sb 200	InAs ₅₀ Sb ₅₀ 100
60	Al ₄₀ In ₆₀ Sb	4000	Al ₄₈ In ₅₂ Sb	500	InAs ₄₀ Sb ₆₀ 1000	Al ₄₈ In ₅₂ Sb 200	Al ₄₀ In ₆₀ Sb 100

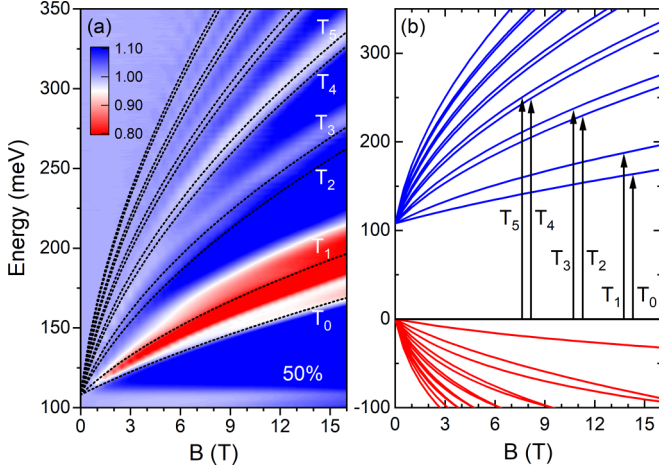


FIG. 2. (a) False color plot of the normalized transmission $T(B)/T(0 \text{ T})$ of the $\text{InAs}_{0.50}\text{Sb}_{0.50}$ alloy sample. The dashed lines indicate the fitting results from the $\mathbf{k} \cdot \mathbf{p}$ model using parameters given in Table II. The first few absorption modes are labeled with T_i , $i = 0, 1, \dots, 5$. (b) Calculated LL fan diagram of $\text{InAs}_{0.50}\text{Sb}_{0.50}$ at the Γ point. The blue, black, and red colors denote the LLs from the EB, HH, and LH bands, respectively. The arrows show the low-lying LL transitions, in correspondence to those in panel (a).

assumptions, the $\mathbf{k} \cdot \mathbf{p}$ Hamiltonian is greatly simplified while, as we will show below, ensuring a good agreement between the experiment and model. The simplified Hamiltonian now reads

$$H_{\mathbf{k}\cdot\mathbf{p}} = \begin{bmatrix} H_+ & 0 \\ 0 & H_- \end{bmatrix}, \quad (1)$$

where

$$H_+ = \begin{bmatrix} E_g & i\sqrt{3}V^\dagger & iV & \sqrt{2}V \\ -i\sqrt{3}V & 0 & 0 & 0 \\ -iV^\dagger & 0 & 0 & 0 \\ \sqrt{2}V^\dagger & 0 & 0 & -\Delta \end{bmatrix},$$

$$H_- = \begin{bmatrix} E_g & -\sqrt{3}V & -V^\dagger & i\sqrt{2}V^\dagger \\ -\sqrt{3}V^\dagger & 0 & 0 & 0 \\ -V & 0 & 0 & 0 \\ -i\sqrt{2}V & 0 & 0 & -\Delta \end{bmatrix}.$$

Here, $V = \frac{1}{\sqrt{6}}P_0k_-$, $\mathbf{k} = (k_x, k_y, k_z)$ is the wave vector, $k_\pm = k_x \pm k_y$, and P_0 is related to the Kane energy by $E_P = 2m_0P_0^2/\hbar^2$. The bases for the Hamiltonian are in the order of the electron band (EB) spin-up, heavy hole (HH) spin-up, light hole (LH) spin-down, split-off (SO) spin-down, EB spin-down, HH spin-down, LH spin-up, and SO spin-up bands.

To calculate the LL energies, we apply the ladder operator formalism and the following ansatz to the two subblocks of the Hamiltonian [31,32]. For the H_+ subblock, the ansatz is $|n_+\rangle = [|n-1\rangle, |n-2\rangle, |n\rangle, |n\rangle]^T$. For the H_- subblock, the ansatz is $|n_-\rangle = [|n-1\rangle, |n\rangle, |n-2\rangle, |n-2\rangle]^T$. Here, $[\dots]^T$ denotes the transpose operation, n is a positive integer, and $|n\rangle$ is the n th harmonic oscillator eigenfunction. Further details of the calculation can be found in Refs. [31,32].

TABLE II. Fitting parameters extracted from experiments using the $\mathbf{k} \cdot \mathbf{p}$ model.

Sb	E_g (eV)	Δ (eV)	E_P (eV)	g_{expt}	g_{theory}
0%	0.415	0.390	19	15.0	12.8
9%	0.315	0.323	22	20.0	21.6
22%	0.220	0.276	20	29.4	31.7
44%	0.132	0.280	19	63.2	63.2
50%	0.108	0.300	19	76.0	87.4
63%	0.100	0.375	21	91.5	108.5
100%	0.235	0.800	23.3	51.3	49.1

With the calculated LLs, we can fit the experimental data and extract the corresponding band parameters. The dashed lines in Fig. 2(a) show the best fits to the data, and Fig. 2(b) shows the calculated LL structure using the fitting parameters in Table II. In Fig. 2(b), we also label out the corresponding low-lying LL transitions for T_0 – T_5 , where we assume the dominant contributions to the observed transitions in Fig. 2(a) are the HH to EB LL transitions [27].

Following the above analysis, we can analyze the experimental results of other InAsSb alloys with different Sb compositions. Figure 3 shows their false color plot of the normalized transmission data for Sb compositions of 9%, 22%, 44%, and 63%, respectively. Similar to Fig. 2(a), the dashed lines are best fits to the data using the $\mathbf{k} \cdot \mathbf{p}$ model, which exhibits excellent agreement with the experiment. Table II summarizes the band parameters extracted from the fitting for different Sb concentrations. We note that the actual fitting parameters are E_g and E_P , whereas Δ does not critically

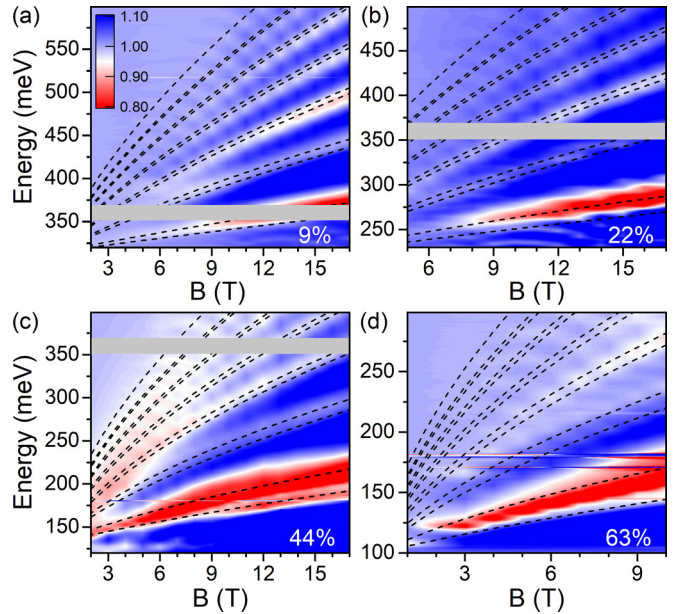


FIG. 3. (a)–(d) False color plot of the normalized transmission $T(B)/T(0 \text{ T})$ for InAsSb samples of (a) 9%, (b) 22%, (c) 44%, and (d) 63% Sb compositions. The dashed lines indicate the fitting results from the $\mathbf{k} \cdot \mathbf{p}$ model using parameters given in Table II. The gray areas are opaque regions to IR light and show no intensity. The color scales in all panels are kept the same.

affect the fitting results as the SO band is distant from the other bands. Here, we assume that Δ follows the bowing relation of ternary InAsSb alloys reported in Ref. [12].

Based on the results in Table II, we can study the bowing effects of the band parameters. First, the band gap E_g bows positively with the Sb concentration. By comparing the inter-band LL transition energies of different compositions, we find that the energy decreases as the Sb composition increases and E_g reaches its minimum ~ 100 meV at 63% Sb concentration. The extracted E_g versus Sb composition gives a bowing coefficient of 0.83, consistent with our previous result [14].

Second, the Kane energy E_p shows a weak bowing effect throughout the entire Sb composition range. This is in contrast to an earlier work [27], where E_p bows significantly with the Sb concentration. It is likely that the samples in Ref. [27] were grown with relaxed strain due to a strong mismatch of the lattice parameters between the substrate and the epilayers, which degraded the quality of the alloys, particularly near the middle of the composition range. According to Ref. [29], this may lead to additional coupling between the conduction and valence bands and hence bowing of E_p .

Lastly, we discuss the bowing effect in g factors. The g factor for the n th LL is defined as $g_n = \min_m |E_{n,\uparrow(\downarrow)}(B) - E_{m,\downarrow(\uparrow)}(B)|/B$, where $\min\{\dots\}$ finds the nearest LL of opposite spin. Based on this definition, the experimental g factors (g_{expt}) are extracted from the splitting of the two lowest EB LLs at 1 T, calculated using the $\mathbf{k} \cdot \mathbf{p}$ model with experimental band parameters. For comparison, we also calculate the theoretical g factors (g_{theory}) from the Roth formula. In both cases, we observe a negative bowing. That is, the g factor gradually increases with increasing Sb composition and reaches a maximum when the band gap reaches a minimum at 63% Sb. Then, the g factor decreases with increasing band gap and Sb composition. Such behavior is expected as the mixing between the EB, HH, and LH bands enhances the g factor, and the mixing is strongly correlated with the size of the band gap. Therefore, the g factors and band gaps exhibit opposite bowing effects. However, the bowing in g_{expt} is found smaller than that in g_{theory} . As discussed before, this is because the Roth formula is a single-band theory and fails to handle the orbital mixing effect as the band gap reduces [8].

Further enhancement of the g factor is possible when the band gap approaches zero. In this case, the EB, HH, and LH bands are degenerated (forming a triple point), and their interactions become the dominant effect. For simplicity, as the SO band is still far from these bands, we can omit the SO band presence in the following discussion. We thus arrive at the following Hamiltonian H_{\pm} :

$$H_+ = \begin{bmatrix} 0 & itU^\dagger & iU \\ -itU & 0 & 0 \\ -iU^\dagger & 0 & 0 \end{bmatrix},$$

$$H_- = \begin{bmatrix} 0 & -tU & -U^\dagger \\ -tU^\dagger & 0 & 0 \\ -U & 0 & 0 \end{bmatrix}.$$

Here, $U = P_0 k_-$, and for a more general discussion, we use t to denote the ratio of the coupling strength between the EB and HH to that between the EB and LH. The corresponding

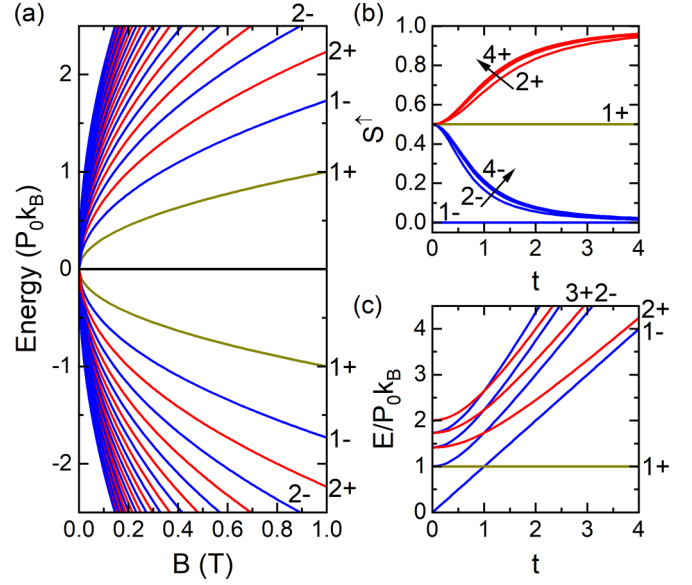


FIG. 4. (a) Landau fan diagram of a triply degenerated band structure (i.e., zero band gap) with $t = \sqrt{3}$ for the case of zinc-blende semiconductors. The energy is in units of $P_0 k_0$, where $k_0 = \sqrt{e/\hbar}$. (b) The spin-up component in low-lying LLs as a function of t . (c) The t dependence of the low-lying LL energies. In all panels, the red and blue colors denote the spin-up and spin-down component dominant LLs, respectively. The dark-yellow color denotes the LLs with equally mixed opposite spins. The black line denotes the highly degenerated HH LLs.

LL energy reads

$$E_{n,\pm}^0 = 0, \quad n = 0, 2, 3, 4, \dots,$$

$$E_{n,+}^\alpha = \alpha P_0 k_B \sqrt{n(1+t^2) - t^2}, \quad n = 1, 2, 3, 4, \dots,$$

$$E_{n,-}^\alpha = \alpha P_0 k_B \sqrt{n(1+t^2) - 1}, \quad n = 1, 2, 3, 4, \dots,$$

where $k_B = \sqrt{eB/\hbar}$, and e is the elementary charge. Each LL has three indices. The superscript α is the band index and takes the value of 0, +1, -1, denoting the HH, EB, and LH bands, respectively. The first subscript n denotes the LL index in each band, and the second subscript \pm denotes the subblock H_{\pm} to which the eigenstate relates. Figure 4(a) shows the magnetic field dependence of the calculated LL energies with $t = \sqrt{3}$, which is the case for III-V semiconductors. Due to the electron-hole symmetry (i.e., $E_{n,\pm}^{-1} = -E_{n,\pm}^{+1}$), we will focus on the $\alpha = +1$ LLs in the discussion below. We will also exclude the discussion of the spin states in the $\alpha = 0$ LLs as their Zeeman effect is negligible due to large degeneracy. In this case, we can omit the band index for simplicity.

As the basis state for each subblock H_{\pm} is not a pure spin state, the spin-up component of a LL is found to be

$$S_{n,+}^\uparrow = 1 - \frac{n/2}{n(1+t^2) - t^2}, \quad S_{n,-}^\uparrow = \frac{(n-1)/2}{n(1+t^2) - 1}.$$

Figure 4(b) shows the calculated spin-up component of the low-lying LLs as a function of t . We find that independent of t , $LL_{1,+}$ is equally spin mixed while $LL_{1,-}$ is fully spin-down polarized. For other LLs, they become more spin polarized

with increasing t . Hence, for t that gives decent spin polarization, the Zeeman splitting is now directly connected to the orbital energy levels (i.e., the LLs) and exhibits a peculiar relativistic \sqrt{B} magnetic field dependence [Fig. 4(a)], in stark contrast to the conventional linear in B Zeeman splitting.

On the other hand, the magnitude of the Zeeman splitting also depends on the choice of t . Figure 4(c) shows the t dependence of the low-lying LL energies. For $t = 0, 1$, and $t \rightarrow +\infty$, the LLs of opposite dominant spin components are degenerated, and thus zero Zeeman effect. On the contrary, when a LL is equally separated from two neighboring LLs of opposite spins, the optimized Zeeman effect is achieved. For example, a simple calculation using the relation $E_{2,-} - E_{2,+} = E_{2,+} - E_{1,-}$ gives an optimized $t \approx 1.7$ for large Zeeman splitting in $LL_{2,+}$, which is close to $t = \sqrt{3}$ in III-V semiconductors. The optimized t for other LLs is also close to this value.

It is interesting to compare the Zeeman effect in such triple-point semimetals to those of Dirac semimetals such as graphene [26] and $ZrTe_5$ [34]. In the two-band model (as in Dirac semimetals), the interaction between the two bands leads to degenerated LLs with no dominant spin components. This is equivalent to taking $t \rightarrow 0$ or $+\infty$ in our model, where no Zeeman effect exists if only considering the orbital interaction. The Zeeman effect comes into play through the interaction with remote bands [8,24,35], which leads to a relatively small g factor. However, in triple-point semimetals, the additional interaction with the third band can lift the degeneracy of the LLs (except for the lowest two LLs). Therefore, the Zeeman effect can reveal itself through the splitting of the orbital energy levels and no longer takes effect through perturbations. In this case, the g factor can be more easily and effectively manipulated through the interactions between the

three bands (EB, HH, and LH) rather than with the remote bands. These observations could be useful in designing high g factors in future topological materials.

Before closing, we comment on how to enhance the Zeeman effect in practicable materials. We find that $t = \sqrt{3}$ is an ideal ratio that gives rise to a decent 80% spin polarization in $n > 1$ LLs as well as the ideal energy spacing between spin-polarized LLs. In fact, this ratio is protected by the crystal symmetry and hence it can be also applied to the zinc-blende type semiconductor [36]. Using a typical value of $E_p = 20$ eV, the Zeeman splitting for $LL_{2,+}$ is about 11 meV at 1 T (i.e., $\min\{E_{2,-} - E_{2,+}, E_{2,+} - E_{1,-}\} \approx 11$ meV), which corresponds to an effective g factor of $g \approx -200$. Our finding is consistent with that reported on triple-point (zinc-blende) HgCdTe [37]. Therefore, zinc-blende type semiconductors with zero energy gap are ideal candidates for realizing large Zeeman effects.

This work was primarily supported by the NSF (Grants No. DMR-1809120 and No. DMR-1809708). The MBE growth at Stony Brook University was also supported by the U.S. Army Research Office (Grant No. W911NF2010109) and Stony Brook Foundation (Quantum Information Science and Technology proto-center). The magneto-IR measurements were performed at the National High Magnetic Field Laboratory, which is supported by the NSF Cooperative Agreement (No. DMR-1644779 and No. DMR-2128556) and the State of Florida. S.M., D.S., and Z.J. acknowledge support from the DOE (for magneto-IR measurements) under Grant No. DE-FG02-07ER46451. Y.J. acknowledges support from the National Natural Science Foundation of China (Grant No. 12274001) and the Natural Science Foundation of Anhui Province (Grant No. 2208085MA09).

-
- [1] I. Žutić, J. Fabian, and S. Das Sarma, Spintronics: Fundamentals and applications, *Rev. Mod. Phys.* **76**, 323 (2004).
- [2] D. D. Awschalom and M. E. Flatté, Challenges for semiconductor spintronics, *Nat. Phys.* **3**, 153 (2007).
- [3] P. Sengupta, C. Khandekar, T. Van Mechelen, R. Rahman, and Z. Jacob, Electron g -factor engineering for nonreciprocal spin photonics, *Phys. Rev. B* **101**, 035412 (2020).
- [4] H. Kosaka, A. Kiselev, F. Baron, K. W. Kim, and E. Yablonovitch, Electron g factor engineering in III-V semiconductors for quantum communications, *Electron. Lett.* **37**, 464 (2001).
- [5] R. M. Lutchyn, E. P. A. M. Bakkers, L. P. Kouwenhoven, P. Krogstrup, C. M. Marcus, and Y. Oreg, Majorana zero modes in superconductor-semiconductor heterostructures, *Nat. Rev. Mater.* **3**, 52 (2018).
- [6] L. M. Roth, B. Lax, and S. Zwerdling, Theory of Optical Magneto-Absorption Effects in Semiconductors, *Phys. Rev.* **114**, 90 (1959).
- [7] C. E. Pryor and M. E. Flatté, Landé g Factors and Orbital Momentum Quenching in Semiconductor Quantum Dots, *Phys. Rev. Lett.* **96**, 026804 (2006).
- [8] M. S. Dresselhaus, G. Dresselhaus, and A. Jorio, *Group Theory: Application to the Physics of Condensed Matter* (Springer Science & Business Media, Berlin, 2007).
- [9] M.-C. Chang and Q. Niu, Berry curvature, orbital moment, and effective quantum theory of electrons in electromagnetic fields, *J. Phys.: Condens. Matter* **20**, 193202 (2008).
- [10] J.-M. Jancu, R. Scholz, E. A. de Andrada e Silva, and G. C. La Rocca, Atomistic spin-orbit coupling and $\mathbf{k} \cdot \mathbf{p}$ parameters in III-V semiconductors, *Phys. Rev. B* **72**, 193201 (2005).
- [11] R. Isaacson, Electron spin resonance in n -type InSb, *Phys. Rev.* **169**, 312 (1968).
- [12] I. Vurgaftman, J. R. Meyer, and L. R. Ram-Mohan, Band parameters for III-V compound semiconductors and their alloys, *J. Appl. Phys.* **89**, 5815 (2001).
- [13] S. P. Svensson, W. L. Sarney, H. Hier, Y. Lin, D. Wang, D. Donetsky, L. Shterengas, G. Kipshidze, and G. Belenky, Band Gap of $InAs_{1-x}Sb_x$ with native lattice constant, *Phys. Rev. B* **86**, 245205 (2012).
- [14] S. Suchalkin, J. Ludwig, G. Belenky, B. Laikhtman, G. Kipshidze, Y. Lin, L. Shterengas, D. Smirnov, S. Luryi, W. L. Sarney, and S. P. Svensson, Electronic properties of unstrained unrelaxed narrow gap $InAs_xSb_{1-x}$ alloys, *J. Phys. D* **49**, 105101 (2016).
- [15] W. Mayer, W. F. Schiela, J. Yuan, M. Hatefipour, W. L. Sarney, S. P. Svensson, A. C. Leff, T. Campos, K. S. Wickramasinghe, M. C. Dartiailh, I. Žutić, and J. Shabani, Superconducting proximity effect in InAsSb surface quantum wells with

- in situ Al contacts, *ACS Appl. Electron. Mater.* **2**, 2351 (2020).
- [16] C. M. Moehle, C. T. Ke, Q. Wang, C. Thomas, D. Xiao, S. Karwal, M. Lodari, V. van de Kerkhof, R. Termaat, G. C. Gardner, G. Scappucci, M. J. Manfra, and S. Goswami, InSbAs two-dimensional electron gases as a platform for topological superconductivity, *Nano Lett.* **21**, 9990 (2021).
- [17] S. Metti, C. Thomas, D. Xiao, and M. J. Manfra, Spin-orbit coupling and electron scattering in high-quality InSb_{1-x} as x quantum wells, *Phys. Rev. B* **106**, 165304 (2022).
- [18] S. Suchalkin, G. Belenky, M. Ermolaev, S. Moon, Y. Jiang, D. Graf, D. Smirnov, B. Laikhtman, L. Shterengas, G. Kipshidze, S. P. Svensson, and W. L. Sarney, Engineering Dirac materials: Metamorphic InAs_{1-x}Sb_x/InAs_{1-y}Sb_y superlattices with ultralow bandgap, *Nano Lett.* **18**, 412 (2018).
- [19] S. Suchalkin, M. Ermolaev, T. Valla, G. Kipshidze, D. Smirnov, S. Moon, M. Ozerov, Z. Jiang, Y. Jiang, S. P. Svensson, W. L. Sarney, and G. Belenky, Dirac energy spectrum and inverted bandgap in metamorphic InAsSb/InSb superlattices, *Appl. Phys. Lett.* **116**, 032101 (2020).
- [20] G. W. Winkler, Q. Wu, M. Troyer, P. Krogstrup, and A. A. Soluyanov, Topological Phases in InAs_{1-x}Sb_x: From Novel Topological Semimetal to Majorana Wire, *Phys. Rev. Lett.* **117**, 076403 (2016).
- [21] A. Rogalski, P. Martyniuk, M. Kopytko, P. Madejczyk, and S. Krishna, InAsSb-based infrared photodetectors: Thirty years later on, *Sensors* **20**, 7047 (2020).
- [22] S. P. Svensson, W. L. Sarney, D. Donetsky, G. Kipshidze, Y. Lin, L. Shterengas, Y. Xu, and G. Belenky, Materials design parameters for infrared device applications based on III-V semiconductors, *Appl. Opt.* **56**, B58 (2017).
- [23] D. Donetsky, J. Liu, G. Kipshidze, L. Shterengas, G. Belenky, W. Sarney, and S. Svensson, InAsSb-based heterostructures for infrared light modulation, *Appl. Phys. Lett.* **115**, 081102 (2019).
- [24] Y. Jiang, M. Ermolaev, G. Kipshidze, S. Moon, M. Ozerov, D. Smirnov, Z. Jiang, and S. Suchalkin, Giant g -factors and fully spin-polarized states in metamorphic short-period InAsSb/InSb superlattices, *Nat. Commun.* **13**, 5960 (2022).
- [25] Y. Jiang, Z. L. Dun, H. D. Zhou, Z. Lu, K.-W. Chen, S. Moon, T. Besara, T. M. Siegrist, R. E. Baumbach, D. Smirnov *et al.*, Landau-level spectroscopy of massive Dirac fermions in single-crystalline ZrTe₅ thin flakes, *Phys. Rev. B* **96**, 041101 (2017).
- [26] Y. Jiang, Z. Lu, J. Gigliotti, A. Rustagi, L. Chen, C. Berger, W. de Heer, C. J. Stanton, D. Smirnov, and Z. Jiang, Valley and Zeeman splittings in multilayer epitaxial graphene revealed by circular polarization resolved magneto-infrared spectroscopy, *Nano Lett.* **19**, 7043 (2019).
- [27] S. N. Smith, C. C. Phillips, R. H. Thomas, R. A. Stradling, I. T. Ferguson, A. G. Norman, B. N. Murdin, and C. R. Pidgeon, Interband magneto-optics of InAs_{1-x}Sb_x, *Semicond. Sci. Technol.* **7**, 900 (1992).
- [28] J. Tersoff, Dislocations and strain relief in compositionally graded layers, *Appl. Phys. Lett.* **62**, 693 (1993).
- [29] E. D. Siggia, $\vec{k} \cdot \vec{p}$ perturbation theory in semiconductor alloys, *Phys. Rev. B* **10**, 5147 (1974).
- [30] G. Belenky, D. Donetsky, G. Kipshidze, D. Wang, L. Shterengas, W. L. Sarney, and S. P. Svensson, Properties of unrelaxed InAs_{1-x}Sb_x alloys grown on compositionally graded buffers, *Appl. Phys. Lett.* **99**, 141116 (2011).
- [31] Y. Jiang, S. Thapa, G. D. Sanders, C. J. Stanton, Q. Zhang, J. Kono, W. K. Lou, K. Chang, S. D. Hawkins, J. F. Klem *et al.*, Probing the semiconductor to semimetal transition in InAs/GaSb double quantum wells by magneto-infrared spectroscopy, *Phys. Rev. B* **95**, 045116 (2017).
- [32] G. D. Sanders, Y. Sun, F. V. Kyrychenko, C. J. Stanton, G. A. Khodaparast, M. A. Zudov, J. Kono, Y. H. Matsuda, N. Miura, and H. Munekata, Electronic states and cyclotron resonance in n -type InMnAs, *Phys. Rev. B* **68**, 165205 (2003).
- [33] B. A. Foreman, Elimination of spurious solutions from eight-band $\mathbf{k} \cdot \mathbf{p}$ theory, *Phys. Rev. B* **56**, R12748(R) (1997).
- [34] J. Wang, Y. Jiang, T. Zhao, Z. Dun, A. L. Miettinen, X. Wu, M. Mourigal, H. Zhou, W. Pan, D. Smirnov *et al.*, Magneto-transport evidence for strong topological insulator phase in ZrTe₅, *Nat. Commun.* **12**, 6758 (2021).
- [35] Z.-D. Song, S. Sun, Y.-F. Xu, S.-M. Nie, H.-M. Weng, Z. Fang, and X. Dai, First principle calculation of the effective Zeeman's couplings in topological materials, in *Memorial Volume for Shoucheng Zhang* (World Scientific, Singapore, 2021), Chap. 11, pp. 263–281.
- [36] L. C. L. Y. Voon and M. Willatzen, *The $k p$ Method: Electronic Properties of Semiconductors* (Springer Science & Business Media, Berlin, 2009).
- [37] M. Orlita, D. Basko, M. Zholudev, F. Teppe, W. Knap, V. Gavrilenko, N. Mikhailov, S. Dvoretiskii, P. Neugebauer, C. Faugeras *et al.*, Observation of three-dimensional massless Kane fermions in a zinc-blende crystal, *Nat. Phys.* **10**, 233 (2014).